

Dust polarization spectral dependence from Planck HFI data

Turning point on CMB polarization foregrounds modelling

Alessia Ritacco^{1,2,3} *, François Boulanger², Vincent Guillet^{3,4}, Jean-Marc Delouis⁵, Jean-Loup Puget^{2,3},
Jonathan Aumont⁶, and Léo Vacher⁶

¹ INAF-Osservatorio Astronomico di Cagliari, Via della Scienza 5, 09047 Selargius, IT

² Laboratoire de Physique de l'École Normale Supérieure, ENS, Université PSL, CNRS, Sorbonne Université, Université de Paris, 75005 Paris, France

³ Institut d'Astrophysique Spatiale, CNRS, Université Paris-Saclay, CNRS, Bât. 121, 91405 Orsay, France

⁴ Laboratoire Univers et Particules de Montpellier, Université de Montpellier, CNRS/IN2P3, CC 72, Place Eugène Bataillon, 34095 Montpellier Cedex 5, France

⁵ Laboratoire d'Océanographie Physique et Spatiale (LOPS), Univ. Brest, CNRS, Ifremer, IRD, Brest, France

⁶ IRAP, Université de Toulouse, CNRS, CNES, UPS, (Toulouse), France

Preprint online version: December 21, 2022

ABSTRACT

The search for the primordial B -modes of the cosmic microwave background (CMB) relies on the separation from the brighter foreground dust signal. In this context, the characterisation of the spectral energy distribution (SED) of thermal dust in polarization has become a critical subject of study. We present a power-spectra analysis of *Planck* data, which improves on previous studies by using the newly released SRoll2 maps that correct residual data systematics, and by extending the analysis to regions near the Galactic plane. Our analysis focuses on the lowest multipoles between $\ell=4$ and 32, and three sky areas with sky fractions of $f_{\text{sky}} = 80\%$, 90% , and 97% . The mean dust SED for polarization and the 353 GHz Q and U maps are used to compute residual maps at 100, 143 and 217 GHz, highlighting variations of the dust polarization SED on the sky and along the line of sight. Residuals are detected at the three frequencies for the three sky areas. We show that models based on total intensity data are underestimating by a significant factor the complexity of dust polarized CMB foreground. Our analysis emphasizes the need to include variations of polarization angles of the dust polarized CMB foreground. The frequency dependence of the EE and BB power spectra of the residual maps yields further insight. We find that the moments expansion to the first order of the modified black-body (MBB) spectrum provides a good fit to the EE power-spectra. This result suggests that the residuals could follow mainly from variations of dust MBB spectral parameters. However, this conclusion is challenged by cross-spectra showing that the residuals maps at the three frequencies are not fully correlated, and the fact that the BB power-spectra do not match the first order moment expansion of a MBB SED. This work sets new requirements for simulations of the dust polarized foreground and component separation methods, showing that a significant refinement to dust modelling is necessary to ensure an unbiased detection of the CMB primordial B -modes at the precision required by future CMB experiments. Further work is also needed to model theoretically the impact of polarization angle variations on EE and BB power spectra of residuals maps.

Key words. CMB - polarization - foregrounds

1. Introduction

One of the outstanding questions in cosmology concerns the existence of primordial gravitational waves as predicted by the theory of cosmic inflation (Guth 1981; Linde 1982). Although the primordial gravitational waves are not directly detectable with foreseen experiments, they are expected to leave an imprint as a curl-like pattern in the cosmic microwave background (CMB) polarization anisotropies, referred to as primordial B -modes, which could be measured. This is a main goal of present and future CMB experiments, including the *LiteBIRD* satellite (LiteBIRD Collaboration et al. 2022), and *BICEP/Keck* (Ade et al. 2022), the *Simons Observatory* (Ade et al. 2019) and *CMB-Stage 4* (Abazajian et al. 2016) from the ground. These experiments aim at measuring the tensor-to-scalar ratio r , which represents the amplitude of the primor-

dial tensor (B -modes) relative to scalar perturbations (E -modes) of the CMB. This parameter, related to the energy scale of inflation, is expected to be in the range between 10^{-2} to 10^{-4} (Kamionkowski & Kovetz 2016; LiteBIRD Collaboration et al. 2022). A very high control and subtraction of instrumental systematic effects and Galactic foregrounds is required for an unbiased measurement of such low r values.

The dust emission represents a major obstacle, because its amplitude is much larger than that of primordial B -modes signal (Planck Collaboration et al. 2020d). In this context, the characterisation of the spectral energy distribution (SED) of dust has become a critical step in the search for B -modes. The *Planck* data have shown that the mean dust SED for polarization and total intensity are very close, and that they are both well fitted by a modified black body (MBB) law (Planck Collaboration et al. 2015, 2020d). In addition, far-IR polarization measurements obtained by

*Corresponding author: A. Ritacco, alessia.ritacco@inaf.it

the *BLASTPol* balloon-borne experiment (e.g., [Ashton et al. 2018](#)), have shown that the dust polarization fraction is roughly constant between 250 μm and 3 mm (100 GHz). These remarkable results suggest that the emission from a single grain type dominates the long-wavelength emission in both polarization and total intensity ([Guillet et al. 2018](#); [Hensley & Draine 2022](#)).

Maps of MBB parameters (dust spectral index and temperature) have been obtained fitting the total intensity *Planck* data (e.g. [Planck Collaboration et al. 2016a,e](#)). The *Planck* 2018 data release (hereafter PR3, [Planck Collaboration et al. 2020c](#)) does not provide comparable constraints on MBB parameters in polarization due to insufficient signal to noise ratio and instrumental systematics ([Osumi et al. 2021](#)). These limiting factors are emphasized by the lack of polarization maps at 545 and 857 GHz to constrain the dust SED. The frequency dependence of dust polarization data also involves polarization angles. Where dust SED and magnetic field orientation vary within the beam, the frequency scaling of the Stokes Q and U parameters may differ ([Ichiki et al. 2019](#); [Vacher et al. 2022b](#)). Integration along the line of sight may therefore induce variations of the polarization angle with frequency ([Tassis & Pavlidou 2015](#); [Planck Collaboration et al. 2017](#)). [Pelgrims et al. \(2021\)](#) provided first observational evidence of this effect analyzing *Planck* data toward lines of sight with multiple velocity components in H I emission. Additional emission components (e.g. magnetic dipole and CO emission ([Puglisi et al. 2017](#))) can also contribute to SED variations ([Hensley & Bull 2018](#)).

SED variations on the sky and along the line of sight induce a decorrelation between dust emission at different frequencies, which is referred to as frequency decorrelation. Attempts to detect frequency decorrelation through a power spectra analysis of the multi-frequency *Planck* data have only yielded upper limits ([Planck Collaboration et al. 2017, 2020d](#)). This work improves on previous studies by using a new upgraded version of *Planck* maps. The polarization maps at frequencies 100 to 353 GHz used in this paper are taken from the SRoll2.0 version of the *Planck* data processing ([Delouis et al. 2019](#)), which correct the data from systematics that plague the PR3 release. This work also improves the sensitivity to frequency decorrelation by extending the analysis from the high Galactic latitude sky regions best suited for CMB observations to brighter regions near the Galactic plane.

The paper is organized as follows. Sect. 2 presents the *Planck* data we use; Sect. 3 introduces the reference models we use for data simulations and analysis. In Sect. 4, we determine the dust mean SED for polarization from 100 to 353 GHz. We quantify spatial variations of the dust polarization SED in Sect. 5 and the contribution of polarization angles in Sect. 6. The frequency dependence is analyzed in Sect. 7. The paper results are summarized in Sect. 8.

2. Planck polarization data and masks

The *Planck* satellite observed the sky in total intensity (also referred as temperature) in the range of frequency of the electromagnetic spectrum from 30 to 857 GHz, and in polarization from 30 to 353 GHz. Data was obtained from two instruments on board the satellite: the Low Frequency Instrument (LFI, [Mennella et al. 2011](#)), and the High

Frequency Instrument (HFI, [Planck HFI Core Team et al. 2011](#)). *Planck* HFI measured the linear polarization at 100, 143, 217, and 353 GHz ([Rosset et al. 2010](#)).

The *Planck* scanning strategy sampled almost all the sky pixels every six months, with alternating scan directions in successive six-month periods. The *Planck* mission includes five surveys, each covering a large fraction of the sky (hereafter f_{sky}). Maps are produced for the full-mission data-set together with the survey, year, and half-mission maps, as reported in [Planck Collaboration et al. \(2016c\)](#).

2.1. SRoll2 maps

In this work, we use sky maps and end-to-end data simulations produced by the SRoll2 software¹. This latter has been developed to improve subtraction of systematic effects. The dominant systematic effect for the polarized signal at 353 GHz in the PR3 maps is related to the poor measurement of the time transfer function of the detectors, while at lower frequencies it is dominated by the non-linearity of the analog-to-digital converters. Both systematics have been greatly improved consistently with all other known effects for the SRoll2 data-set ([Delouis et al. 2019](#)).

Hereafter $Q_P(\nu)$ and $U_P(\nu)$ are the *Planck* polarization maps at frequency ν , including the CMB, dust and synchrotron as well as noise and systematics. We use the *Planck* HFI maps at 100, 143, 217 and 353 GHz. We limit our data analysis to polarization at low multipoles ($4 < \ell < \ell_{\text{max}}=32$) and work with HEALPix pixelization ([Górski et al. 2005](#)) at $N_{\text{side}}=32$ (i.e. map pixel size of 1.8°). In order to obtain these maps, we follow [Planck Collaboration et al. \(2016d\)](#) and [Planck Collaboration et al. \(2020a\)](#) degrading the full-resolution maps first to $N_{\text{side}}=1024$, to ease the computation, and next to $N_{\text{side}}=32$ applying the following cosine filter in harmonic space ([Benabed et al. 2009](#)):

$$f(\ell) = \begin{cases} 1, & \ell \leq N_{\text{side}}; \\ \frac{1}{2} \left(1 + \sin \left(\frac{\pi}{2} \frac{\ell}{N_{\text{side}}} \right) \right), & N_{\text{side}} < \ell < 3N_{\text{side}}; \\ 0, & \ell \geq 3N_{\text{side}}. \end{cases} \quad (1)$$

All the maps used in this study and presented in the paper have been degraded to $N_{\text{side}}=32$ by following this approach.

2.2. Subtraction of synchrotron emission

The 100 and 143 GHz maps include non-negligible synchrotron emission that we subtract to focus our data analysis on the dust emission. Hence, we define the following maps

$$\begin{aligned} Q'_P(\nu) &= Q_P(\nu) - Q_s(\nu) \\ U'_P(\nu) &= U_P(\nu) - U_s(\nu), \end{aligned} \quad (2)$$

where $[Q_s, U_s](\nu)$ are estimates of the synchrotron Stokes parameters. Notice that the $Q'_P(\nu)$ and $U'_P(\nu)$ maps include the CMB. Hereafter the prime superscript is used to indicate Stokes maps where the synchrotron emission is subtracted or absent.

We use synchrotron template maps at $\nu_s = 30$ GHz, as obtained by the *Commander* component separation

¹The SRoll2 maps are available [here](#) and the simulations [here](#)

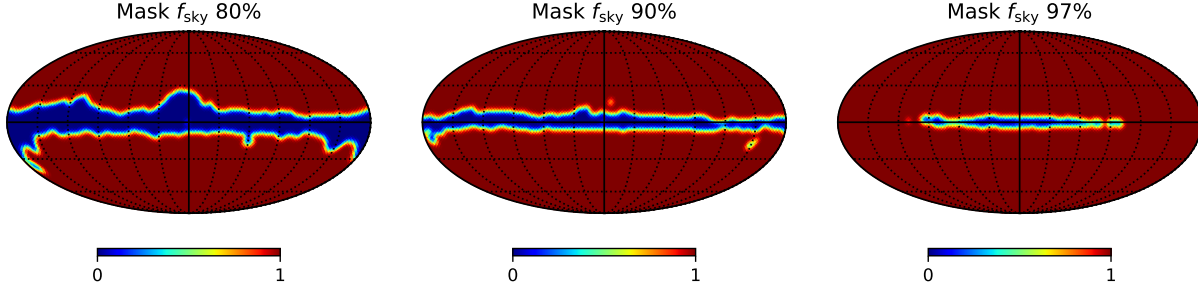


Fig. 1. From left to right apodized masks for $f_{\text{sky}}=80$, 90, and 97 %.

(Planck Collaboration et al. 2016a) applied to PR3 *Planck* maps. To extrapolate from 30 to 100 and 143 GHz, we use a single spectral index β_s , uniform over the sky, to extrapolate synchrotron polarization from 30 to $\nu = [100, 143]$ GHz.

$$[Q, U]_s(\nu) = [Q, U]_s(\nu_s) \cdot C_v^{\text{CC}_s} \cdot C_v^{UC_{RJ}} \cdot \left(\frac{\nu}{30 \text{ GHz}}\right)^{\beta_s}, \quad (3)$$

where the $[Q, U]_s(\nu)$ maps are in K_{CMB} and $[Q, U]_s(\nu_s)$ in K_{RJ} ; $C_v^{UC_{RJ}}$ is the conversion factor from K_{RJ} to K_{CMB} , and $C_v^{\text{CC}_s}$ the color correction, at frequency ν . The conversion factor values at 100 and 143 GHz are listed in Tab. 1.

To determine β_s , we use spectral indices derived by Martire et al. (2022), from a detailed analysis combining *Planck* and *WMAP* (Bennett et al. 2013) data at 30 and 23 GHz, respectively. Table 4 in Martire et al. (2022) lists spectral indices derived from *EE* and *BB* power spectra. We combine the two pairs of *EE* and *BB* spectral indices, for the two largest sky areas with $f_{\text{sky}} = 94$ and 70 %, to compute a mean value, weighted by inverse squared uncertainties, $\beta_s = -3.19 \pm 0.07$.

This mean value is a reasonable approximation considering recent studies that obtained a synchrotron spectral index in polarization β_s of: i) -3.22 ± 0.08 over the southern sky (Krachmalnicoff et al. 2018); ii) -3.17 ± 0.06 in the North Polar Spur (Svalheim et al. 2020); and iii) -3.25 ± 0.06 within the BICEP2/Keck survey footprint (Weiland et al. 2022). The study of de la Hoz (2022) hints at evidence of spatial variations of β_s , which would need to be accounted for in future developments.

ν [GHz]	100	143	217	353
$C_v^{\text{CC}_d}$	1.09	1.02	1.12	1.11
$C_v^{UC_K}$	244.1	371.7	483.7	287.4
$C_v^{UC_{RJ}}$	1.26	1.69		
$C_v^{\text{CC}_s}$	0.9797	0.9504		
ρ_ν	1.005	0.98	1.015	1

Table 1. Unit conversions $C_v^{UC_{RJ}, UC_K}$ and colour corrections $C_v^{\text{CC}_{d,s}}$ as taken from Planck Collaboration et al. (2014c). The factor $\rho(\nu)$ is the correction to the polarization efficiencies (Planck Collaboration et al. 2020c,d).

2.3. Sky masks and power spectra

We compute power spectra for three sky areas presented in Fig. 1 with sky fractions f_{sky} of 80 %, 90 % and 97 %. We

use larger f_{sky} than what is usually done to study Galactic foregrounds in order to increase the signal-to-noise ratio. To mask areas of bright dust emission, we use the dust optical depth map estimated at 353 GHz by fitting a modified blackbody (MBB) spectral model to the GNILC (generalized needlet internal linear combination (GNILC, Planck Collaboration et al. 2016f)) dust maps at 353, 545, 857, and the IRAS 3000 GHz map (Fixsen et al. 1999). We smooth the map with a 5° beam before reducing the HEALPix resolution to $N_{\text{side}}=32$. Next, we sort the pixels by increasing amplitude to define the appropriate masks to obtain $f_{\text{sky}} = 80$ %, 90 %, and 97 %. Finally, we smooth again the mask maps to 5° beam resolution, in order to apodize them and avoid edge effects on the Galactic cut contours.

The power spectra are computed by using the *PolSpice* estimator, which corrects for multipole-to-multipole coupling and for the mixing of the *E*- and *B*- modes due to the sky masking (Chon et al. 2004). We systematically compute cross-power spectra to have no bias from data noise. To compute power spectra at one given frequency, we use the so-called “half-mission” maps (hereafter “HM”). Notice that most of the residual instrumental systematic effects evolve with time and are decorrelated between the two half-mission data sets. Throughout the paper, we use $\mathcal{D}_\ell \equiv \ell(\ell+1)C_\ell/2\pi$ where C_ℓ is the original angular power spectrum.

3. Reference models and data simulations

In our analysis of the *Planck* data, we make use of two reference models of the dust emission and of data simulations, which we introduce in this section.

3.1. Reference models

The *Planck* data analysis has shown that the MBB emission law fits well the SED of the dust emission for total intensity (Planck Collaboration et al. 2014a, 2016a) and polarization (Planck Collaboration et al. 2020d). This provides a convenient and commonly used parametrization of the dust SED:

$$I_d(\nu) = C_v^{UC_K} \cdot C_v^{\text{CC}_d}(\beta_d, T_d) \cdot \rho_\nu \cdot \tau_{\nu_0} \left(\frac{\nu}{\nu_0}\right)^{\beta_d} \cdot B_\nu(T_d) \quad (4)$$

where $B_\nu(T_d)$ is the Planck function; T_d , β_d and τ_{ν_0} are the dust temperature, spectral index and optical depth maps at the reference frequency ν_0 , respectively. The MBB emission is expressed in MJy sr^{-1} whereas the data are in thermodynamic units. The conversion between the two is ac-

accomplished by two factors. The first, $C_v^{\text{UC}_K}$, is a unit conversion from MJy sr^{-1} to K_{CMB} for the reference spectral dependence: constant product νI_ν over the bandpass. The second, $C_v^{\text{CC}_d}(\beta_d, T_d)$, is the colour correction accounting for the difference between the reference spectral dependence and the MBB spectrum. This correction depends on the MBB parameters: β_d and T_d , which are taken equal to 1.53 and 19.6 K, respectively (Planck Collaboration et al. 2020d). The estimated values are presented in Tab. 1.

In Planck Collaboration et al. (2020c), the polarization efficiencies have been adjusted, within the uncertainties of the ground calibration, in order to match cosmological parameters derived from CMB polarization with the ones obtained from CMB temperature (Planck Collaboration et al. 2020c). The factor ρ_ν in Eq. 4 represents this correction to the polarization efficiencies. We use the same values as Planck Collaboration et al. (2020d), which are listed in Tab. 1. The uncertainty on ρ_ν is estimated to be 0.5% at $\nu=[100, 143, 217]$ GHz. The correction could not be estimated with the required accuracy at 353 GHz.

We apply Eq. 4 to two sets of MBB parameters derived from *Planck* component separations methods: i) the GNILC method using maps corrected for anisotropies of the cosmic infrared background, and ii) the standard Bayesian analysis framework, implemented in the *Commander* code (Planck Collaboration et al. 2016a). For GNILC, T_d , β_d and τ_{ν_0} have been obtained by fitting a MBB model on the dust total intensity at the *Planck* frequencies 353, 545 and 857 GHz and IRAS 3000 GHz, while the *Commander* fit includes all *Planck* frequencies, together with the 9-year WMAP observations between 23 and 94 GHz (Bennett et al. 2013) and a 408 MHz survey map (Haslam et al. 1982).

To build our reference models, we assume that the dust SED is the same for total intensity and polarization, an hypothesis supported by the close match between the total intensity and polarization SEDs (Planck Collaboration et al. 2015, 2020d), which we aim to further test in this paper. For GNILC, we also assume that the MBB fitted over the far-IR may be extrapolated to microwave frequencies (Planck Collaboration et al. 2014b). Within this framework, the Stokes parameters $Q_d(\nu)$ and $U_d(\nu)$ at $\nu = [100, 143, 217]$ GHz may be computed from the *Planck* maps at $\nu_0 = 353$ GHz:

$$\begin{aligned}
 Q_d(\nu) &= \frac{I_d(\nu)}{I_d(\nu_0)} \cdot (Q_P(\nu_0) - Q_{P,\text{CMB}}) \\
 U_d(\nu) &= \frac{I_d(\nu)}{I_d(\nu_0)} \cdot (U_P(\nu_0) - U_{P,\text{CMB}}),
 \end{aligned} \quad (5)$$

where $Q_{P,\text{CMB}}$ and $U_{P,\text{CMB}}$ are CMB Stokes maps from *Planck*. We use the *Planck* SMICA CMB maps (Planck Collaboration et al. 2020e). Our *Commander* and GNILC models are low resolution versions of dust models in PySM (Thorne et al. 2017; Zonca et al. 2021), which are commonly used by the CMB community.

3.2. Data simulations

In order to account for the *Planck* satellite noise including instrumental systematics and CMB signal we compute a set of simulated maps as:

$$\begin{aligned}
 Q'_{\text{sim}}(\nu) &= Q_d(\nu) + Q_{\text{noise+syst}}(\nu) + Q_{\text{CMB}} \\
 U'_{\text{sim}}(\nu) &= U_d(\nu) + U_{\text{noise+syst}}(\nu) + U_{\text{CMB}},
 \end{aligned} \quad (6)$$

where $[Q_{\text{noise+syst}}, U_{\text{noise+syst}}]$ are the 200 SRoll2 simulations to which we subtract the *Planck* sky model that contain synchrotron, dust and CMB in order to isolate *Planck* noise/systematics, (see Delouis et al. 2019, for more details). And $[Q_{\text{CMB}}, U_{\text{CMB}}]$ are 200 independent realizations of the CMB computed from the theoretical power spectra of the best-fit Λ CDM model to the *Planck* data ² (Planck Collaboration et al. 2020b), with the r parameter equal to 0. Thus, Eq. 6 yields 200 realizations of the reference model maps.

In Fig. 2 we present one realization of the *Commander* Q'_{sim} and U'_{sim} maps at 100, 143, and 217 GHz. In Fig. 3, the power spectra of the dust model *Commander*, the synchrotron template at the two lowest frequencies, the CMB and a simulation of the SRoll2 noise plus systematics are compared. The mean values $\langle D_\ell \rangle_{\ell=[4,32]}$ for EE (diamonds) and BB (squares) spectra are plotted versus frequency for the three values of f_{sky} .

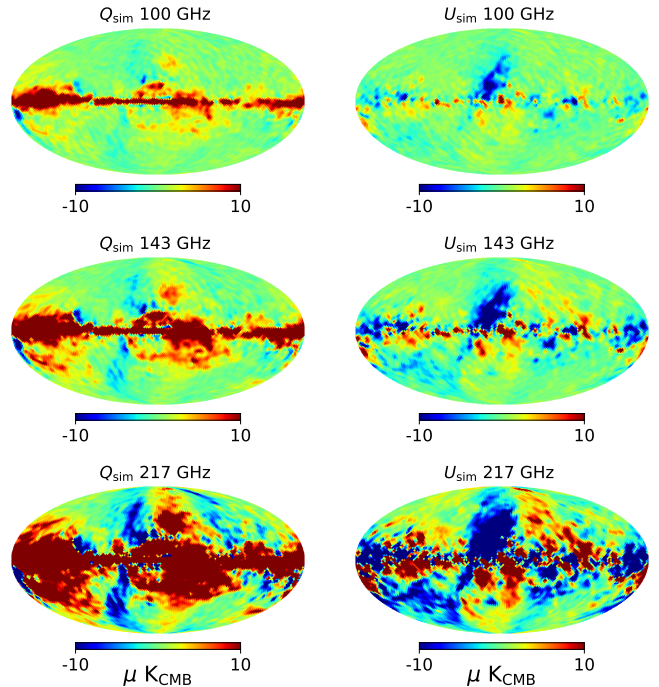


Fig. 2. Q'_{sim} and U'_{sim} reference maps for 100 GHz (top), 143 GHz (middle), and 217 GHz (bottom) as obtained for the *Commander* reference model.

4. Dust mean SED in polarization

In this section, we derive the mean SED of dust polarization. We use *Planck* polarization maps at 100, 143, 217 and 353 GHz. The SED values are normalized to the reference frequency $\nu_0 = 353$ GHz.

We follow earlier studies (Planck Collaboration et al. 2016b, 2020d) using cross power spectra to determine the dust mean polarized SED for *Planck* data $\gamma_P(\nu)$, the reference models $\gamma_d(\nu)$ and the simulations $\gamma_{\text{sim}}(\nu)$ normalized to ν_0 as:

²We used the data file COM_PowerSpect_CMB-base-plikHM-TTTEEE-lowl-lowE-lensing-minimum-theory_R3.01.txt available on the *Planck* Legacy archive.

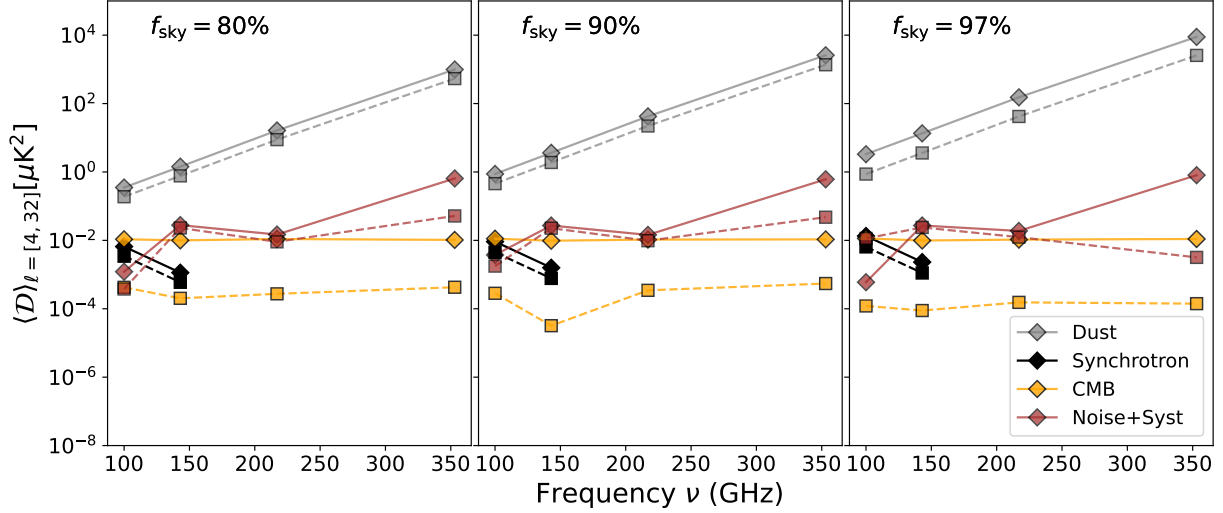


Fig. 3. Amplitudes, averaged for $4 < \ell < 32$, of the $\mathcal{D}_\ell EE$ (diamond) and BB (square) power spectra versus frequency. Each plot presents the spectra of the *Commander* dust model (gray), our synchrotron estimate at 100 and 143 GHz (black), the CMB (orange), and the SRoll2 noise plus systematics (light brown). The three plots from left to right correspond to $f_{\text{sky}} = 80, 90$ and 97% .

$$\begin{aligned} \gamma_P^{XX}(\nu) &= \rho_\nu \left\langle \frac{\mathcal{D}_\ell^{XX}(\nu \times \nu_0) - \mathcal{D}_{\ell, \text{CMB}}^{XX}}{\mathcal{D}_\ell^{XX}(\nu_0 \times \nu_0) - \mathcal{D}_{\ell, \text{CMB}}^{XX}} \right\rangle_{\ell_{\min}, \ell_{\max}} \\ \gamma_d^{XX}(\nu) &= \left\langle \frac{\mathcal{D}_{\ell, d}^{XX}(\nu \times \nu_0)}{\mathcal{D}_{\ell, d}^{XX}(\nu_0 \times \nu_0)} \right\rangle_{\ell_{\min}, \ell_{\max}} \\ \gamma_{\text{sim}}^{XX}(\nu) &= \rho_\nu \left\langle \frac{\mathcal{D}_{\ell, \text{sim}}^{XX}(\nu \times \nu_0) - \mathcal{D}_{\ell, \text{CMB}}^{XX}}{\mathcal{D}_{\ell, \text{sim}}^{XX}(\nu_0 \times \nu_0) - \mathcal{D}_{\ell, \text{CMB}}^{XX}} \right\rangle_{\ell_{\min}, \ell_{\max}} \end{aligned} \quad (7)$$

where

$$\begin{aligned} \mathcal{D}_\ell^{XX}(\nu \times \nu_0) &= [\mathcal{Q}_p^{\text{HM1}}(\nu), U_p^{\text{HM1}}(\nu)] \times [\mathcal{Q}_p^{\text{HM2}}(\nu_0), U_p^{\text{HM2}}(\nu_0)] \\ \mathcal{D}_{\ell, d}^{XX}(\nu \times \nu_0) &= [\mathcal{Q}_d^{\text{HM1}}(\nu), U_d^{\text{HM1}}(\nu)] \times [\mathcal{Q}_d^{\text{HM2}}(\nu_0), U_d^{\text{HM2}}(\nu_0)] \\ \mathcal{D}_{\ell, \text{sim}}^{XX}(\nu \times \nu_0) &= [\mathcal{Q}_{\text{sim}}^{\text{HM1}}(\nu), U_{\text{sim}}^{\text{HM1}}(\nu)] \times [\mathcal{Q}_{\text{sim}}^{\text{HM2}}(\nu_0), U_{\text{sim}}^{\text{HM2}}(\nu_0)] \end{aligned} \quad (8)$$

and $\mathcal{D}_{\ell, \text{CMB}}^{XX}$ is the CMB power spectrum for the Λ CDM fiducial *Planck* model (Planck Collaboration et al. 2020b) with $XX \in [EE, BB]$. $\mathcal{D}_\ell^{XX}(\nu_0 \times \nu_0)$ is computed with $\nu = \nu_0$ in Eq. 8. The symbol $\langle \rangle$ indicates the cross-power spectrum operator and $\langle \rangle$ the arithmetic mean over the ℓ -range from $\ell_{\min} = 4$ to $\ell_{\max} = 32$. Notice that in the denominator of the first and third equations of Eq. 7, we omit ρ_{ν_0} because it is equal to 1. Tab. 4 lists the SED values $\gamma_P(\nu)$ for the *Planck* data and $\gamma_d(\nu)$ for the reference models, for both *EE* and *BB* and for the three sky areas. The uncertainties $\sigma_{\gamma_P}(\nu)$ are derived from the standard deviation of the 200 *Planck* simulations. The uncertainty on the polarization efficiencies ρ_ν and the synchrotron spectral index β_s are propagated through our analysis and their contribution to the total error-bar are added to σ_{γ_P} .

The dust SEDs *Planck* γ_P are presented in Fig. 4. The values are normalized to a MBB SED with $\beta_d = 1.53$ and $T_d = 19.6$ K (Planck Collaboration et al. 2014b, 2015). Notice that the value at 353 GHz is always equals to unity because it is the reference frequency considered for our analysis, see Eq. 7. The colour corrections $C_\nu^{\text{CCd}}(\beta_d=1.53$ and $T_d=19.6\text{K})$ are those listed in Tab. 1. The figure shows that the $\gamma_P(\nu)$ values are consistent with the MBB used

for normalization within 5 %, in agreement with previous results (Planck Collaboration et al. 2015, 2020d). Some of the differences could be due to systematics that plagues PR3 data. Note that subtracting synchrotron emission primarily affects the value of the *EE* signal to 100 GHz. Though its level is low, around 2 to 3%. For the mask at 97% we observe a significant difference between $\gamma_P^{EE}(\nu)$ and $\gamma_P^{BB}(\nu)$ that we interpret with variations of the SED within the beam, which do not average in the same way for *EE* and *BB*. These variations depend also on the mask and could be more important when the analysis includes a significant part of the Galactic plane.

Fig. 5 shows the ratio between γ_d for the *Commander* (top) and GNILC (bottom) models and γ_P . For *Commander* we observe a very close match between $\gamma_P(\nu)$ and $\gamma_d(\nu)$ at 143 and 217 GHz for $f_{\text{sky}}=80$ and 90 % and both *EE* and *BB* signals. For GNILC the match is not as good, in particular we observe a significant difference for $f_{\text{sky}}=80\%$ at 100 and 143 GHz. For $f_{\text{sky}}=97\%$ we observe a difference between the *EE* and *BB* values at 100 GHz. Apart for this latter we observe that $\gamma_d(\nu)$ values are consistent within 5% with the $\gamma_P(\nu)$ values. All the differences between γ_P γ_d may be due to averaging effects along the line of sight.

This analysis shows that assuming a reference model based on total intensity data could not completely reproduce the SED observed in polarization data, thus biasing any CMB polarization *E*-modes and *B*-modes signals if used as reference for component separation methods. In order to ensure an unbiased detection of the CMB polarization, at the precision required from future CMB experiments, we need to address these very small spatial SED variations of the dust polarization emission.

5. Spatial variations of the polarization SED

In this section, we characterize the spatial variations of the dust SED in polarization and quantify the degree of correlation with variations of the dust SED in total intensity.

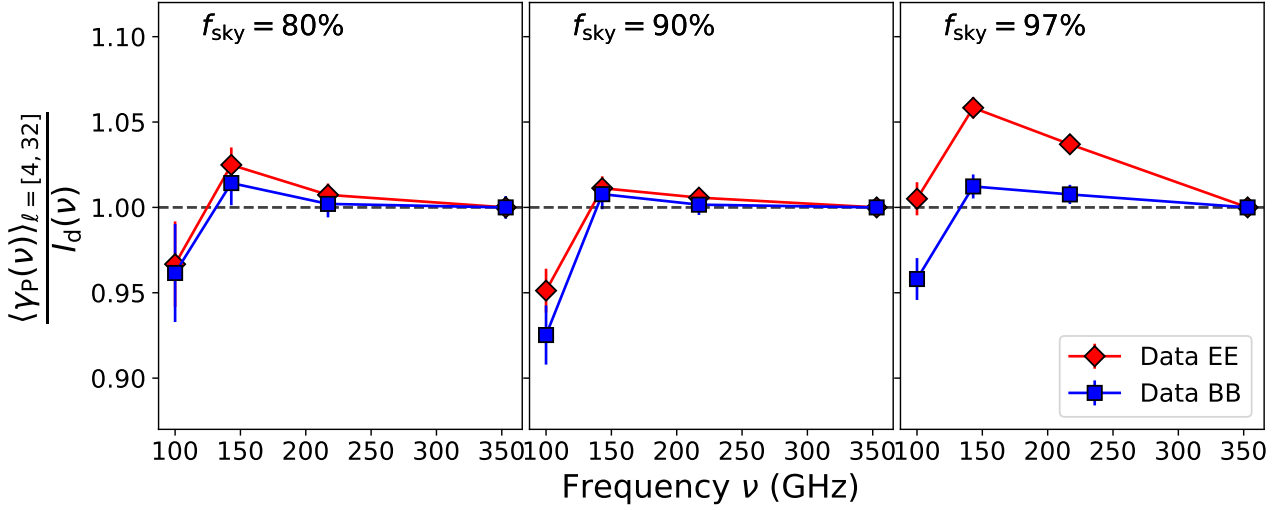


Fig. 4. Dust mean SED $\gamma_P(\nu)$ normalized by a modified black body function $I_d(\nu)$ with fixed $\beta_d = 1.53$ and $T_d = 19.6$ K as given by Planck Collaboration et al. (2020d) and accounting for color corrections. *EE* and *BB* values are shown in red and blue, respectively. From left to right the results are presented for $f_{\text{sky}} = [80, 90, 97]\%$.

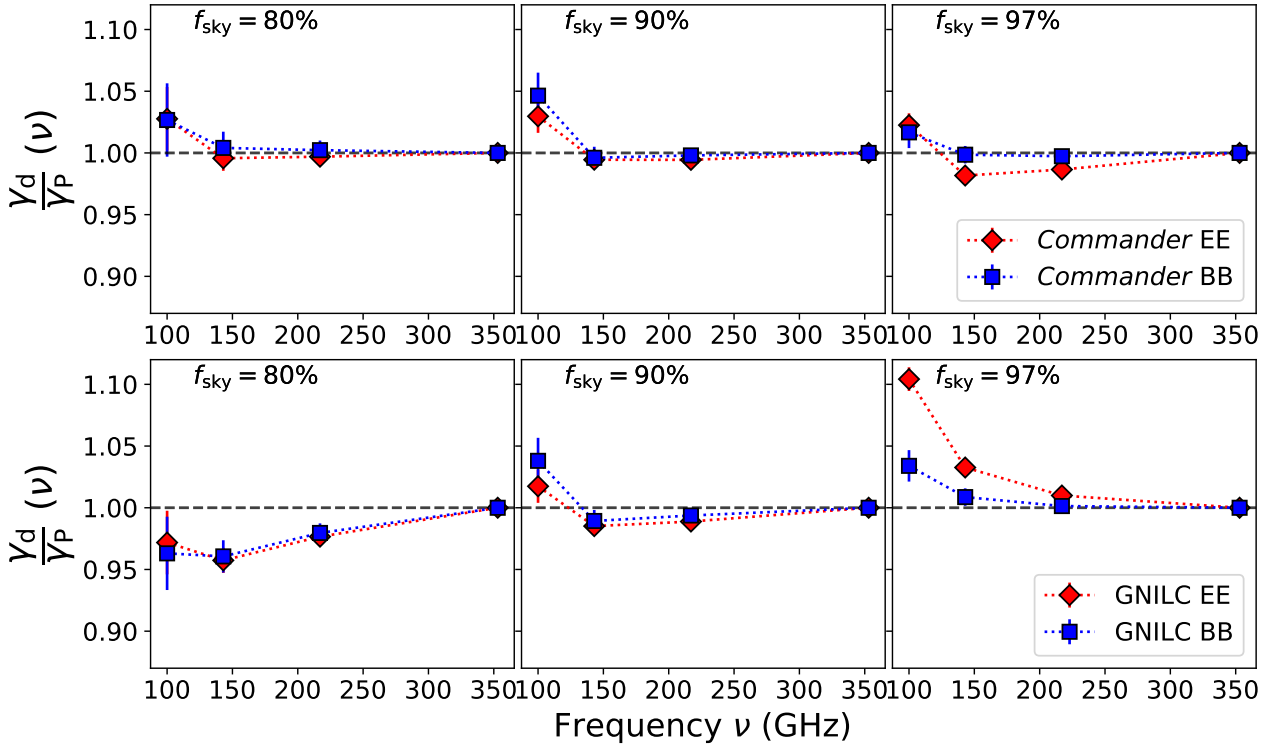


Fig. 5. Dust mean SED $\gamma_d(\nu)$ computed for the reference models (*Commander* (top row) and *GNILC* (bottom row)). *EE* and *BB* values are shown in red and blue, respectively. From left to right the results are presented for $f_{\text{sky}} = [80, 90, 97]\%$. All values are normalized by the $\gamma_P(\nu)$ values obtained from the data and shown in Fig. 4.

5.1. Residual maps

To quantify the spatial variations of the dust SED, we compute differences between the *Planck* frequency maps at 100, 143 and 217 GHz and the 353 GHz scaled by the mean dust SED $\gamma_P(\nu)$ from Sect. 4, that we approximate to the value of $\gamma_P^{EE}(\nu)$ because the dust polarization is dominated by *E*-modes. Fig. 4 shows that $\gamma_P^{EE}(\nu) \approx \gamma_P^{BB}(\nu)$ for $f_{\text{sky}} = 80\%, 90\%$. A difference between the two coefficients $\gamma_P(\nu)$ is instead detected for $f_{\text{sky}} = 97\%$. This difference indicates a

correlation between dust emission properties and the structure of the magnetized interstellar medium. However, we have checked that our approximation does not significantly impact the results also for this f_{sky} . The three maps $R_Q(\nu)$ and $R_U(\nu)$ computed as:

$$R_Q(\nu) = Q'_P(\nu) - \gamma_P(\nu) \cdot Q_P(\nu_0) \quad (9)$$

$$R_U(\nu) = U'_P(\nu) - \gamma_P(\nu) \cdot U_P(\nu_0)$$

with $\nu = 100, 143$ and 217 GHz, and $\nu_0 = 353$ GHz to which hereafter we refer as residual maps, are shown in Fig. 6. For

f_{sky}	80%			90%			97%		
$\nu[\text{GHz}]$	100	143	217	100	143	217	100	143	217
γ_{p}^{EE}	0.0181	0.0400	0.1276	0.0178	0.0392	0.1274	0.0188	0.0411	0.1314
$\gamma_{\text{d}}^{EE} \text{ Commander}$	0.0187	0.0388	0.1291	0.0185	0.0382	0.1286	0.0194	0.0395	0.1315
$\gamma_{\text{d}}^{EE} \text{ GNILC}$	0.0177	0.0373	0.1265	0.0182	0.0379	0.1279	0.0209	0.0416	0.1347
error	0.0005	0.0003	0.0005	0.0002	0.0002	0.0003	0.0002	0.0001	0.0002
γ_{p}^{BB}	0.0180	0.0394	0.1269	0.0173	0.0391	0.1269	0.0180	0.0393	0.1276
$\gamma_{\text{d}}^{BB} \text{ Commander}$	0.0186	0.0387	0.1291	0.0182	0.0382	0.1285	0.0183	0.0384	0.1292
$\gamma_{\text{d}}^{BB} \text{ GNILC}$	0.0174	0.0371	0.1262	0.0181	0.0379	0.1279	0.0187	0.0388	0.1297
error	0.0005	0.0005	0.0008	0.0003	0.0003	0.0004	0.0002	0.0002	0.0003

Table 2. Dust mean SED values for the *Planck* polarization data $\gamma_{\text{p}}(\nu)$ and the reference models $\gamma_{\text{d}}(\nu)$. The uncertainty is estimated as standard deviation over 200 simulations. For 100 and 143 GHz the uncertainty accounts for the error associated with the synchrotron template subtraction.

comparison, we also compute difference maps for the reference models (see Eq. 10) and simulations maps replacing $\gamma_{\text{p}}(\nu)$ by $\gamma_{\text{d}}(\nu)$ in Eq. 9.

$$\begin{aligned}
 R_{\text{Qd}}(\nu) &= Q_{\text{d}}(\nu) - \gamma_{\text{d}}(\nu) \cdot Q_{\text{d}}(\nu_0) \\
 R_{\text{Ud}}(\nu) &= U_{\text{d}}(\nu) - \gamma_{\text{d}}(\nu) \cdot U_{\text{d}}(\nu_0) \\
 R_{\text{Q}'_{\text{sim}}}(\nu) &= Q'_{\text{sim}}(\nu) - \gamma_{\text{d}}(\nu) \cdot Q'_{\text{sim}}(\nu_0) \\
 R_{\text{U}'_{\text{sim}}}(\nu) &= U'_{\text{sim}}(\nu) - \gamma_{\text{d}}(\nu) \cdot U'_{\text{sim}}(\nu_0)
 \end{aligned} \tag{10}$$

Notice that, for illustration purpose, all the residual maps shown in Fig. 6, 7, 8 consider a $\gamma_{\text{p}}(\nu)$ and $\gamma_{\text{d}}(\nu)$ in Eq. 9 computed for $f_{\text{sky}} = 90\%$.

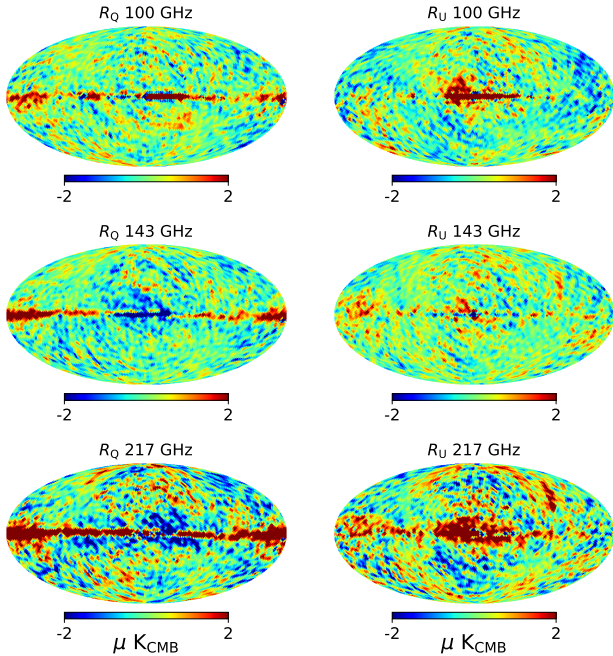


Fig. 6. From top to bottom residual maps R_Q (left) and R_U (right) at 100, 143 and 217 GHz.

One set of simulation maps [$R_{\text{Q}'_{\text{sim}}}(\nu)$, $R_{\text{U}'_{\text{sim}}}(\nu)$] for the *Commander* model is displayed in Fig. 7. The comparison between Figs. 6 and 7 is hampered by *Planck* data noise but one can notice some common features and some differences. In Fig. 6, we also note differences between frequencies among the R_Q and R_U residual maps, in contrast

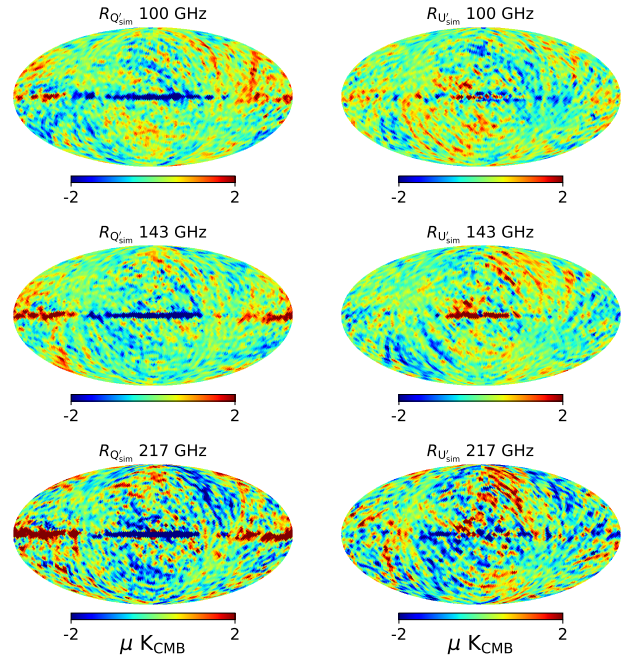


Fig. 7. From top to bottom residual maps for one realization of $R_{\text{Q}'_{\text{sim}}}$ (left) and $R_{\text{U}'_{\text{sim}}}$ (right) obtained for the *Commander* reference model, at 100, 143, 217 GHz respectively.

to what is observed for $R_{\text{Q}'_{\text{sim}}}$ and $R_{\text{U}'_{\text{sim}}}$ in Fig. 7. To illustrate that some of the structures are above data noise and uncorrected systematics, in Fig. 8 we present the independent R_Q and R_U residual half-mission HM1 and HM2 maps estimated at 217 GHz.

This qualitative examination of the maps suggests that we observe SED variations in the residual $R_Q(\nu)$, $R_U(\nu)$ maps, which cannot be simply attributed to SED variations in total intensity, as assumed in the reference models.

5.2. Power spectra analysis

To characterize SED variations, we compute power spectra of residual maps and cross-power spectra with the reference models. We compute two cross-power spectra between (i) independent residual maps [$R_Q^{\text{HM1,HM2}}(\nu)$, $R_U^{\text{HM1,HM2}}(\nu)$], and (ii) between [$R_Q^{\text{HM1}}(\nu)$, $R_U^{\text{HM1}}(\nu)$] and the reference model residuals [$R_{\text{Qd}}^{\text{HM2}}(\nu)$, $R_{\text{Ud}}^{\text{HM2}}(\nu)$]. The 200 simulations are used

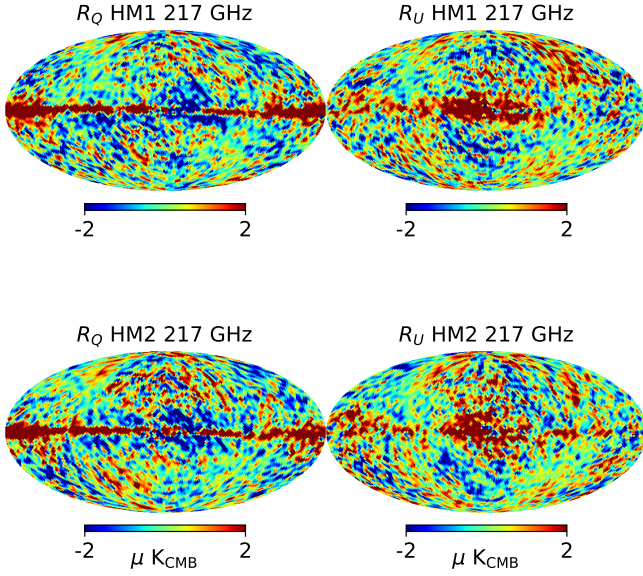


Fig. 8. From left to right, residual maps R_Q (left) and R_U (right) at 217 GHz for two data sets HM1 (top), HM2 (bottom), respectively.

to assess the impact of data noise plus uncorrected systematics and of the CMB on our analysis.

$$\begin{aligned} \mathcal{D}_{\ell,\text{res}}^{\text{XX}}(\nu) &= [R_Q^{\text{HM1}}(\nu), R_U^{\text{HM1}}(\nu)] \times [R_Q^{\text{HM2}}(\nu), R_U^{\text{HM2}}(\nu)] \\ \mathcal{D}_{\ell,\text{d,res}}^{\text{XX}}(\nu) &= [R_Q^{\text{HM1}}(\nu), R_U^{\text{HM1}}(\nu)] \times [R_Q^{\text{HM2}}(\nu), R_U^{\text{HM2}}(\nu)] \\ \mathcal{D}_{\ell,\text{sim,res}}^{\text{XX}}(\nu) &= [R_{Q_{\text{sim}}}^{\text{HM1}}(\nu), R_{U_{\text{sim}}}^{\text{HM1}}(\nu)] \times [R_{Q_{\text{sim}}}^{\text{HM2}}(\nu), R_{U_{\text{sim}}}^{\text{HM2}}(\nu)] \end{aligned} \quad (11)$$

where $\text{XX} \in [EE, BB]$. Fig. 9 shows both sets of cross power spectra for EE (red) and BB (blue) at 100, 143 and 217 GHz for $f_{\text{sky}} = 90\%$. The data points over the ℓ -range 4 to 32 are compared with the 1σ and 2σ dispersion (dark and light gray shades) obtained with the 200 simulations including noise and CMB anisotropies (see Sect. 3.2). In all plots, individual data points have a low signal-to-noise ratio and it is necessary to average them to quantify mean amplitudes and their frequency dependence. The averaged cross power spectra values are computed as:

$$\begin{aligned} A_{\text{res}}(\nu) &= \langle \mathcal{D}_{\ell,\text{res}}^{\text{XX}}(\nu) - (1 - \gamma_P(\nu))^2 \cdot \mathcal{D}_{\ell,\text{CMB}}^{\text{XX}} \rangle_{\ell_{\min}, \ell_{\max}} \\ A_{\text{res,d}}(\nu) &= \langle \mathcal{D}_{\ell,\text{d,res}}^{\text{XX}}(\nu) \rangle_{\ell_{\min}, \ell_{\max}} \\ A_{\text{res,sim}}(\nu) &= \langle \mathcal{D}_{\ell,\text{sim,res}}^{\text{XX}}(\nu) - (1 - \gamma_P(\nu))^2 \cdot \mathcal{D}_{\ell,\text{CMB}}^{\text{XX}} \rangle_{\ell_{\min}, \ell_{\max}} \end{aligned} \quad (12)$$

with $\text{XX} \in [EE, BB]$. Notice that the CMB has been partially subtracted in Eqs. 9, 10. The remaining contribution is accounted for by the term $(1 - \gamma_P(\nu))^2 \cdot \mathcal{D}_{\ell,\text{CMB}}^{\text{XX}}$. In Fig. 10 we plot the amplitudes $A_{\text{res}}(\nu)$ normalized by the mean polarized intensity at reference frequency over each sky area defined as:

$$P_{v_0} = \sqrt{[Q_{\text{HM1}} \cdot Q_{\text{HM2}} + U_{\text{HM1}} \cdot U_{\text{HM2}}]} \quad (13)$$

where HM1 and HM2 refer to the two half-mission maps. We checked that the bias on this estimator of the polarized intensity is negligible at 353 GHz for $N_{\text{side}}=32$. This normalization allows us to compare the results for the three different masks. Absolute values of the residuals may be obtained by scaling the figure data points by $\langle P_{v_0}^2 \rangle = [2453.6,$

5950.5, 13814.3] K_{CMB} for $f_{\text{sky}} = 80\%$, 90% , and 97% respectively. We will discuss the frequency dependence later, here we focus on the comparison with the models. Fig. 11 shows the dust models residuals $A_{\text{res,d}}(\nu)$ normalized by $A_{\text{res}}(\nu)$. The mean amplitudes $A_{\text{res,sim}}(\nu)$ are also computed for each of the 200 simulations and their dispersion provides the error bars. For the 80 and 90% masks, the $A_{\text{res}}(\nu)$ are a factor of about 10 times larger than $A_{\text{res,d}}(\nu)$. For these, uncertainties associated with the chance correlation between the CMB and the dust residuals may thus be somewhat underestimated. For the 97% mask, this difference is smaller. At 143 and 217 GHz, the amplitudes even coincide for the GNILC model. These results show that the reference model only accounts for a minor fraction of the total polarization SED variations in the 80 and 90% masks but a much more significant one for the brighter dust emission in the Galactic plane. Furthermore Fig. 10 highlights the significant variation of BB residuals at 100 GHz toward higher galactic latitudes. Although both EE and BB variation are very small, in the case of $f_{\text{sky}}=80\%$ A_{res}^{BB} represents 0.4% of the total amplitude w.r.t 0.1% detected for A_{res}^{EE} . This feature does not match the residuals extrapolated from the models considered, see Fig. 11 for comparison.

To give a more quantitative estimate we translate the amplitude $A_{\text{res}}(\nu)$ in terms of an effective dispersion of the dust spectral index σ_β , using the following formula based on a first order expansion of the MBB emission law in Mangilli et al. (2021).

$$\sigma_\beta(\nu) = (A_{\text{res}}^{EE}(\nu) + A_{\text{res}}^{BB}(\nu))^{0.5} \cdot \left(\gamma_P(\nu) \cdot P_{v_0} \cdot \left| \ln \left(\frac{\nu}{\nu_0} \right) \right| \right)^{-1} \quad (14)$$

The values of σ_β are listed in Table 3 for the three sky areas and frequencies. These numbers of about 0.1 must be considered as an estimate of the variance of residuals in terms of pure variation of β . These results are consistent with previous studies at low latitude (Planck Collaboration et al. 2016f).

6. Residuals from polarization angles

In this section, we quantify variations of the dust polarization angles as a function of frequency. To do this we introduce the maps

$$\begin{aligned} \tilde{Q}(\nu) &= \gamma_P(\nu) \cdot P(v_0) \times \cos(2\psi(\nu)) \\ \tilde{U}(\nu) &= \gamma_P(\nu) \cdot P(v_0) \times \sin(2\psi(\nu)) \end{aligned} \quad (15)$$

where $P(v_0)$ is the polarized intensity as estimated in Eq. 13, and $\psi(\nu) = \frac{1}{2} \arctan \left(\frac{U}{Q} \right)$ is the polarization angle.

To assess the contribution of variations of ψ to the total $A_{\text{res}}(\nu)$ values, we compute residual maps also for $\tilde{Q}(\nu)$ and $\tilde{U}(\nu)$ as:

$$\begin{aligned} \tilde{R}_Q(\nu) &= \tilde{Q}(\nu) - \gamma_P(\nu) \cdot \tilde{Q}(v_0) \\ \tilde{R}_U(\nu) &= \tilde{U}(\nu) - \gamma_P(\nu) \cdot \tilde{U}(v_0) \end{aligned} \quad (16)$$

The power spectra analysis is performed with these residual maps as described in the previous section:

$$\begin{aligned} \tilde{\mathcal{D}}_{\ell,\text{res}}^{\text{XX}}(\nu) &= [\tilde{R}_Q^{\text{HM1}}(\nu), \tilde{R}_U^{\text{HM1}}(\nu)] \times [\tilde{R}_Q^{\text{HM2}}(\nu), \tilde{R}_U^{\text{HM2}}(\nu)] \\ \tilde{\mathcal{D}}_{\ell,\text{sim,res}}^{\text{XX}}(\nu) &= [\tilde{R}_{Q_{\text{sim}}}^{\text{HM1}}(\nu), \tilde{R}_{U_{\text{sim}}}^{\text{HM1}}(\nu)] \times [\tilde{R}_{Q_{\text{sim}}}^{\text{HM2}}(\nu), \tilde{R}_{U_{\text{sim}}}^{\text{HM2}}(\nu)] \end{aligned} \quad (17)$$

And then the averaged amplitudes are defined as:

$$\tilde{A}_{\text{res}}(\nu) = \langle \tilde{\mathcal{D}}_{\ell,\text{res}}^{\text{XX}}(\nu) - \langle \tilde{\mathcal{D}}_{\ell,\text{sim,res}}^{\text{XX}}(\nu) \rangle_{\text{sim}} \rangle_{\ell_{\min}, \ell_{\max}}, \quad (18)$$

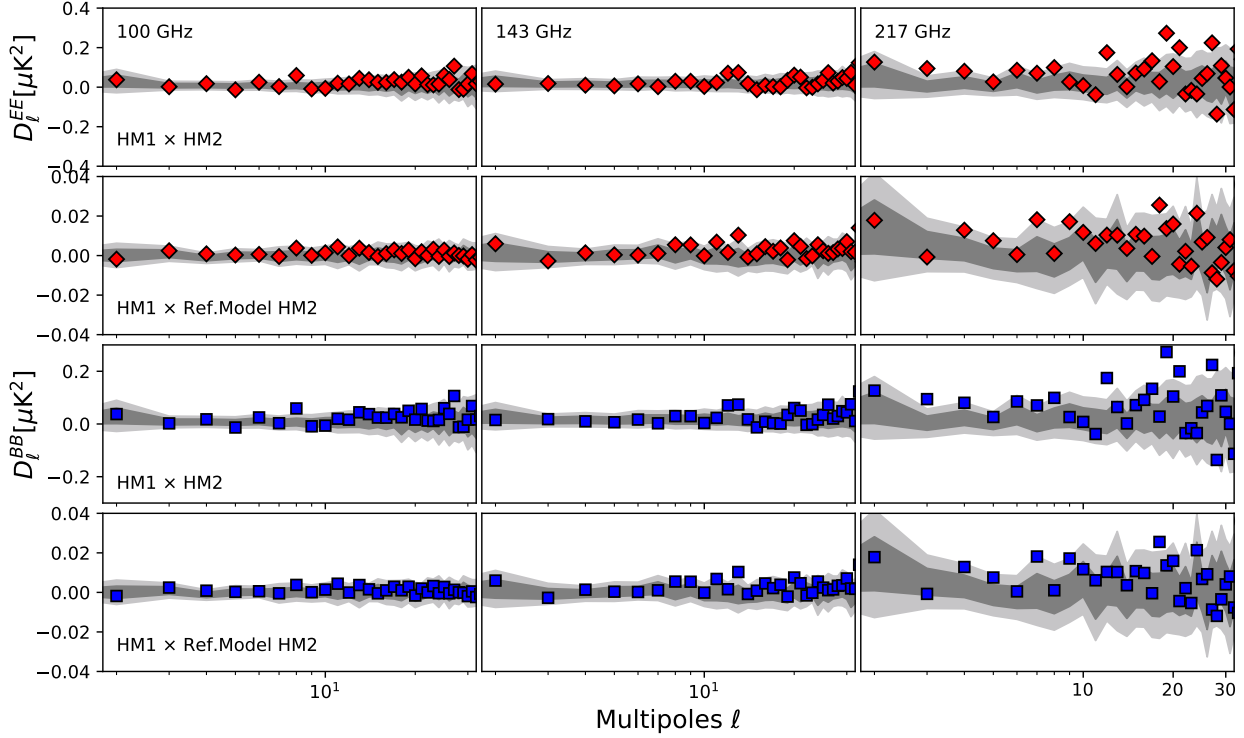


Fig. 9. Cross power spectra correlation $\mathcal{D}_\ell^{\text{xx}}(\nu)$ and $\mathcal{D}_{\ell,d}^{\text{xx}}(\nu)$ indicated as HM1 \times HM2 and HM1 \times Ref.model HM2, respectively, in the labels. Results for $f_{\text{sky}}=90\%$ and *Commander* reference model are shown. From top to bottom the first two rows show the \mathcal{D}_ℓ^{EE} and the last two the \mathcal{D}_ℓ^{BB} cross power spectra, respectively. From left to right the results at 100, 143, and 217 GHz are shown. The dark and light gray shades represent the 1σ and 2σ standard deviation computed from the data simulations.

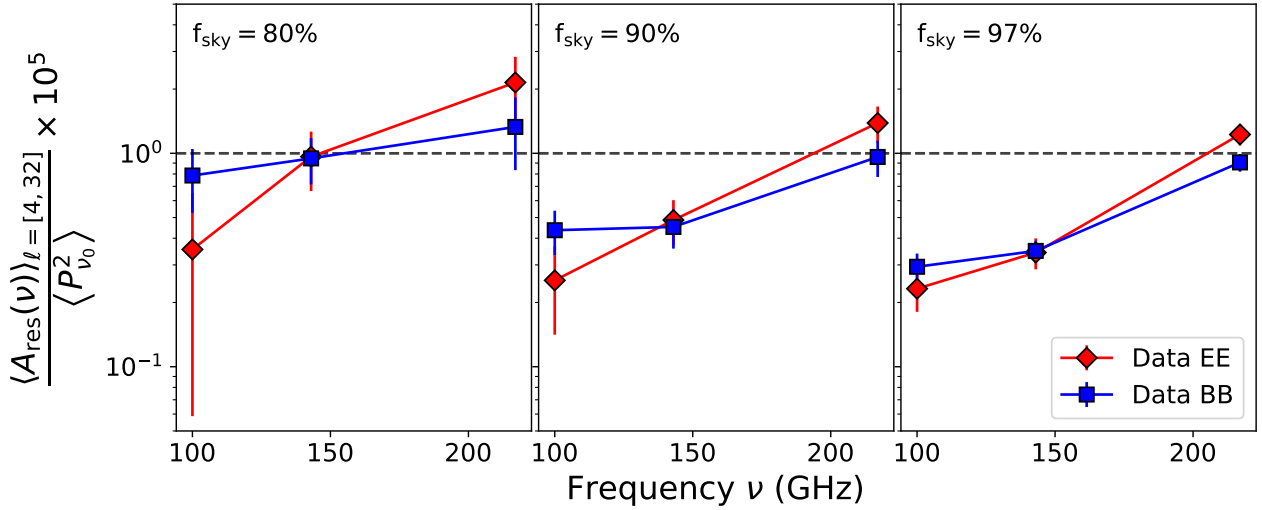


Fig. 10. Amplitudes $A_{\text{res}}(\nu)$ for *EE* (red) and *BB* (blue), respectively. These values are averages over the ℓ -range 4 to 32 and normalized by the mean of $P_{\nu_0}^2$. From left to right results for $f_{\text{sky}}=[80, 90, 97]\%$ are shown.

f_{sky}	80%			90%			97%		
$\nu[\text{GHz}]$	100	143	217	100	143	217	100	143	217
σ_β	0.15 ± 0.03	0.12 ± 0.01	0.09 ± 0.02	0.12 ± 0.02	0.09 ± 0.01	0.08 ± 0.01	0.10 ± 0.01	0.07 ± 0.01	0.07 ± 0.01
δ_ψ	2.71 ± 0.46	1.60 ± 0.25	0.81 ± 0.19	2.43 ± 0.29	1.13 ± 0.15	0.66 ± 0.11	2.33 ± 0.20	0.83 ± 0.09	0.48 ± 0.07

Table 3. Effective dispersion of the dust spectral index σ_β and effective angle variation δ_ψ . Notice that a systematic uncertainty on the polarization angle of 1° must be considered as upper limit on the *Planck* polarization absolute accuracy (Rosset et al. 2010).

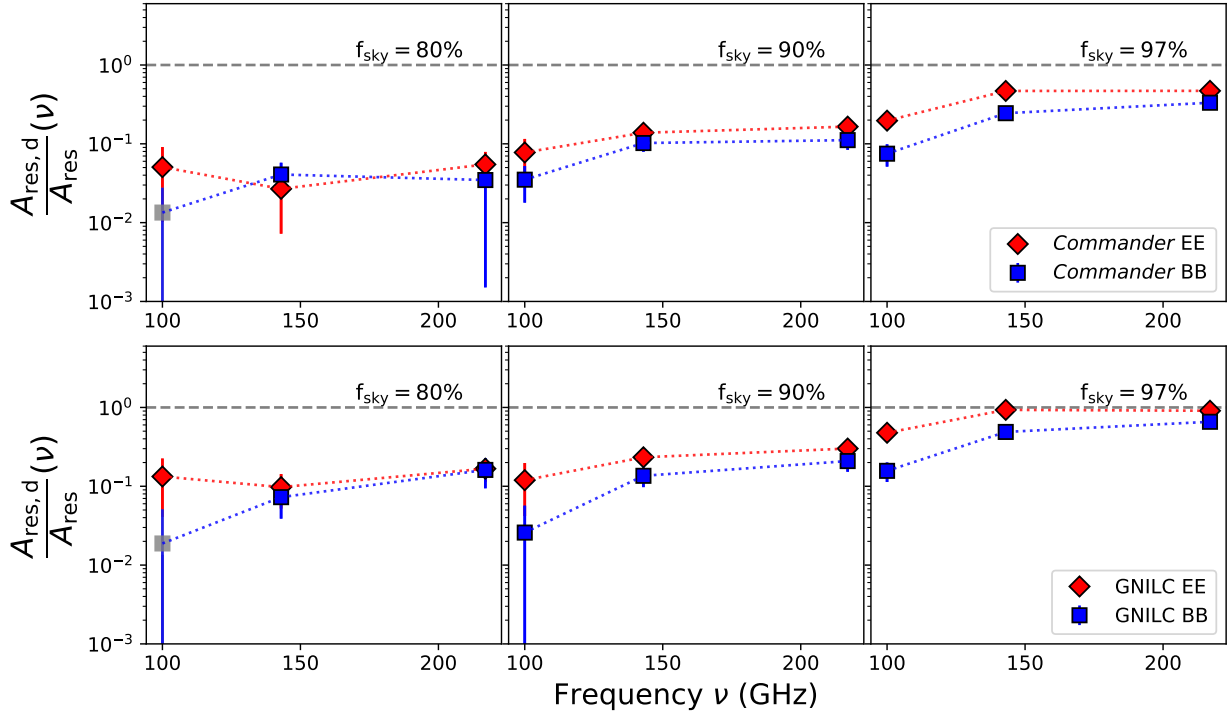


Fig. 11. Residual amplitudes $A_{\text{res},d}(\nu)$ obtained for the reference models *Commander* (top) and *GNILC* (bottom). Red and blue colors represent the *EE* and *BB* results, respectively. These values are estimated by averaging between ℓ -range 4 to 32 and normalizing to the amplitudes of the residuals obtained from the *Planck* data $A_{\text{res}}(\nu)$. See Eq. 12 for details. From left to right results for $f_{\text{sky}}=[80, 90, 97]\%$ are shown. In gray color it is represented the absolute value of *BB* negative results found at 100 GHz for $f_{\text{sky}}=80\%$.

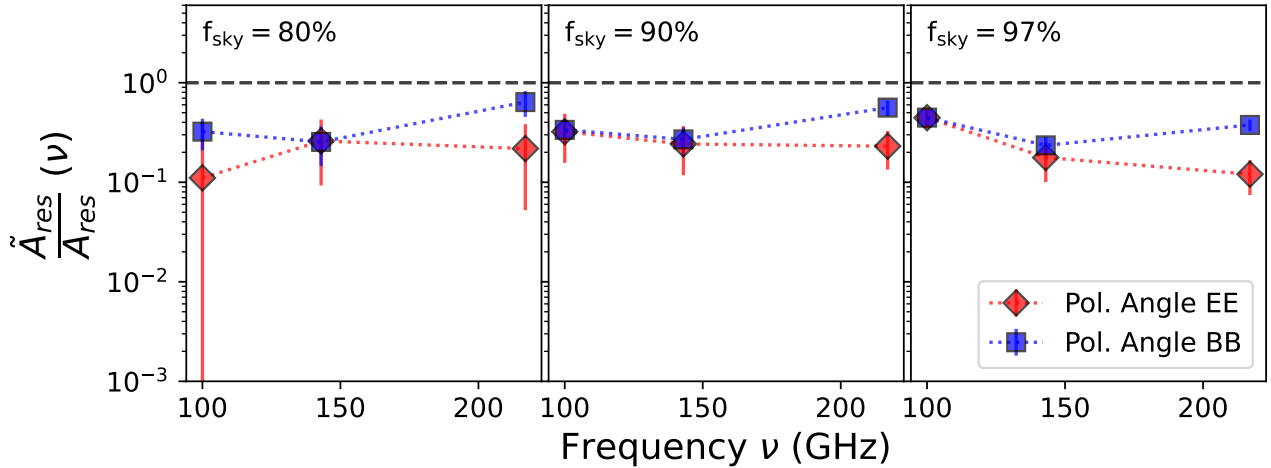


Fig. 12. Amplitudes of the residuals $\tilde{A}_{\text{res}}(\nu)$ obtained by isolating the effect of the polarization angle variation are shown for *EE* (red) and *BB* (blue) (see Eq. 18). These values are normalized to the residual amplitudes obtained from the *Planck* data analysis $A_{\text{res}}(\nu)$. From left to right values for $f_{\text{sky}}=80, 90$, and 97% are shown.

where the second term is used for the CMB and residual noise and systematics debiasing. As in Sect. 5.2 for A_{res} , the uncertainties on \tilde{A}_{res} are derived from the dispersion of the values obtained for the simulations.

Figure 12 compares $\tilde{A}_{\text{res}}(\nu)$ values to $A_{\text{res}}(\nu)$. We find that variations of the polarization angle contribute significantly to the total polarization residuals. The differences observed with f_{sky} may result from the integration along the line of sight or from the limit of our debiasing method,

or both. Indeed, for decreasing Galactic latitudes, the line of sight crosses an increasing number of coherent turbulent cells, and the impact of the magnetic field structure on observed polarization angles may average out.

To express the amplitude $\tilde{A}_{\text{res}}(\nu)$ in terms of an effective angle variation δ_{ψ} , we assume that the residuals results from a systematic angle change over the full sky area. This calculation is just indicative because we do not think that this is a valid assumption. Using equations detailed by Abitbol et al.

(2016), we obtain:

$$\sin \delta_\psi(\nu) = 0.5 \left(\tilde{A}_{\text{res}}^{EE}(\nu) + \tilde{A}_{\text{res}}^{BB}(\nu) \right)^{0.5} \gamma_P^{-1}(\nu) (\langle P_v^2 \rangle)^{-0.5} \quad (19)$$

The values of δ_ψ are listed in Table 3 for three sky areas and frequencies. These values are small but larger than the 1° uncertainty on the ground calibration of the *Planck* absolute polarization angle (Rosset et al. 2010) at both 100 and 143 GHz. The analysis of the *Planck* data confirms this upper limit of 1° (see Fig. 20 in Delouis et al. (2019)).

7. Frequency dependence

In this section, we discuss the frequency dependence of the amplitudes of the residuals power spectra plotted in Fig. 10.

We follow earlier studies (Chluba et al. 2017; Désert 2022) using a Taylor expansion of the MBB emission law to model the residuals. The moment expansion has been applied to dust power spectra in total intensity by Mangilli et al. (2021) and to dust *B*-modes power spectra considered as an intensity by Azzoni et al. (2021) and Vacher et al. (2022a). Within this framework, the power spectra of the residual maps is modelled using the first order expansion as

$$\begin{aligned} \mathcal{D}_\ell(\nu) = \gamma_P(\nu)^2 \cdot \left\{ \begin{array}{l} \text{1st order } \beta \left\{ + \mathcal{D}_\ell^{\beta_1 \times \omega_1^\beta} \ln \left(\frac{\nu}{\nu_0} \right)^2 \right. \\ \text{1st order } T \left\{ + \mathcal{D}_\ell^{T_1 \times \omega_1^T} (\Theta_\nu(T_d) - \Theta_{\nu_0}(T_d))^2 \right. \\ \text{1st order } T \times \beta \left\{ + 2 \mathcal{D}_\ell^{\beta_1 \times \omega_1^T} \ln \left(\frac{\nu}{\nu_0} \right) \cdot (\Theta_\nu(T_d) - \Theta_{\nu_0}(T_d)) \right\}, \end{array} \right. \quad (20) \end{aligned}$$

where $\mathcal{D}_\ell^{a \times b}$ are three moment coefficients introduced by Mangilli et al. (2021) and Vacher et al. (2022a), which are associated with spatial variations of the dust spectral index and temperature, and correlated variations of these two MBB parameters. The $\Theta_\nu(T_d)$ function is the derivative of the logarithm of the black-body spectrum with respect to temperature T_d :

$$\Theta_\nu(T_d) = \frac{x}{T_d} \frac{e^x}{e^x - 1}, \quad (21)$$

where $x = \frac{h\nu}{k_B T_d}$. The temperature T_d is the one used to normalize $\gamma_P(\nu)$ in Fig. 4.

Ichiki et al. (2019) and more extensively Vacher et al. (2022b) have extended the moment expansion to polarization to model the frequency dependence of Stokes *Q* and *U* maps. In the formalism introduced by Vacher et al. (2022b), the moments are spin-2 objects that characterize the frequency dependence of both polarized intensity and polarization angle. This formalism has not yet been applied to *EE* and *BB* power spectra. Qualitatively, one expects that variations of polarization angles induce an exchange of power between *E*- and *B*-modes, which is not symmetric due to the *E/B* asymmetry of dust polarization. The frequency dependence of *EE* and *BB* power spectra of residual maps are thus coupled but not necessarily identical.

In Fig. 13, we present fits of the $A_{\text{res}}^{EE}(\nu)$ with the three terms in Eq. 20, which we refer to f_1 , f_2 and f_3 for β , T and $T \times \beta$, respectively. Over the frequency range of our data analysis from 100 to 217 GHz, these three functions differ

only slightly. The f_1 function provides the best fit, especially for $f_{\text{sky}} = 97\%$, but the fits do not allow us to disentangle the contributions from variations of β_d , T_d and their correlation to the power-spectra of the residual maps.

It is satisfactory to find that the moments expansion to the first order provides a good model for the *EE* power-spectra of residual maps. This result suggests that the residuals follow mainly from variations of dust spectral parameters. However, one can see in the Figure that the fits would not be as good for the *BB* amplitudes, in particular for $f_{\text{sky}} = 80\%$ where the amplitudes do not increase with increasing frequency.

Fig. 13 includes amplitudes derived from the 100×143, 100×217 and 143×217 cross-spectra that are plotted with smaller symbols. These data points are not used in the fit because their values depend on frequency decorrelation. We do find that the residual maps at the three frequencies are not fully correlated. The 143×217 and to a lesser extent the 100×217 amplitudes lie under the model fit. Part of this mismatch could result from a miscalibration of the absolute polarization angle at 217 GHz. To investigate this possibility we performed the following test. We rotated the reference frame of the Q_p and U_p maps at 217 GHz by an angle $\psi = \pm 1^\circ$, which is an upper limit based on the *Planck* polarization absolute angle uncertainty (Delouis et al. 2019). We repeated our analysis with these rotated Stokes maps at 217 GHz for both the *Planck* data and the simulations to correct for the impact of the rotation on the CMB signal. We found that the amplitudes of 100×217 and 143×217 do not change coherently for neither *EE* and *BB*, nor for the three masks considered. We conclude from this test that the mismatch between the spectral model and the cross-spectra amplitudes cannot be explained by a miscalibration of the polarization angle in the *Planck* 217 GHz data.

8. Conclusions

Power spectra of the *Planck* data are used to characterize spatial variations of the polarized dust SED. We improve the sensitivity of previous studies by using the newly released SRoll2 maps and extending the analysis to regions near the Galactic plane. Our analysis focuses on the lowest multipoles between $\ell=4$ and 32, and three sky areas with $f_{\text{sky}} = 80\%$, 90%, and 97%. Maps of MBB parameters from the *Commander* and GNILC component separation methods applied to the *Planck* total intensity data are used as reference models. The main results of our analysis are as follows.

- We confirm earlier studies finding that the mean SED for dust polarization from 100 to 353 GHz is very close to that for total intensity, and to a MBB spectrum with a spectral index $\beta_d=1.53$ for an assumed dust temperature of $T_d = 19.6\text{K}$.
- The mean SED and the 353 GHz *Q* and *U* maps are used to compute residual maps at 100, 143 and 217 GHz, which quantify spatial variations of the dust polarization SED. Residuals are detected at the three frequencies for the three sky areas. The *EE* and *BB* spectra of the residual maps are of comparable amplitude. They do not reproduce the *E/B* asymmetry observed for the total dust power.
- The residual maps are correlated with the reference *Commander* and GNILC models, but this correlation

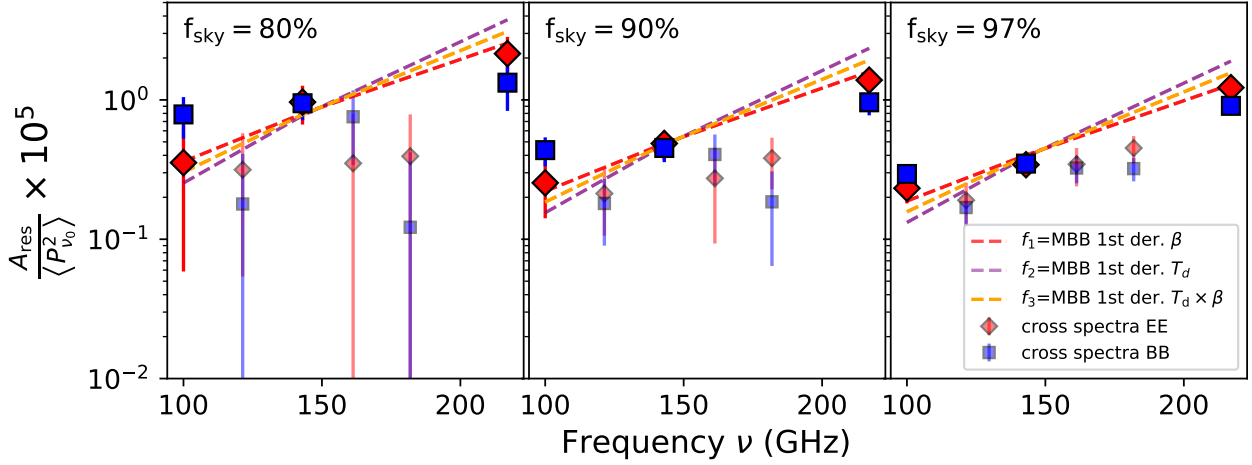


Fig. 13. From left to right residual amplitudes $A_{\text{res}}(\nu)$ (dark markers) EE (red) and BB (blue) for $f_{\text{sky}}=[80,90,97]\%$, are shown. A fit to the data EE accounting for the three components of the moment expansion modelling, separately, described in Eq. 20 is shown in dashed line. Cross power spectra correlation between pair of frequencies: 100×143, 100×217 and 143×217 in smaller and lightened markers, is shown.

accounts for only a fraction of the residuals amplitude. Further, we find that this fraction decreases toward high Galactic latitudes (i.e. for a decreasing f_{sky}). This result shows that models based on total intensity data are underestimating the complexity of dust polarized CMB foreground. Possibly, future developments of *Commander* and *GNILC* models, also accounting for the latest releases of the *Planck* data, could improve the comparison with polarized data.

- To gain insight on the origin of SED variations, we quantify variations in the polarization angle. For $f_{\text{sky}} = 80\%$ and 90% , we find that the contribution of polarization angles to the residuals is dominant, in particular for the BB signal. These results emphasize the importance to consider the geometrical properties of Galactic polarization in component separation.
- The frequency dependence of the EE and BB residual amplitudes yields further insights. We find that the moments expansion to the first order of the MBB spectrum provides a good fit to the EE amplitudes. This result suggests that the residuals follow mainly from variations of dust spectral parameters (temperature and spectral index). However, this conclusion is challenged by the BB results, in particular for $f_{\text{sky}} = 80\%$, and by cross-spectra that show that the residuals maps at the three frequencies are not fully correlated. Further work is needed to model theoretically the impact of polarization angle variations on EE and BB power spectra of residual maps, which we expect to depend on the correlation between dust emission properties and the structure of the magnetized interstellar medium.

Our analysis of *Planck* data brings out significant differences between dust polarization EE and BB SEDs and with respect to total intensity, setting new requirements for simulations of the dust polarized foreground and component separation methods. A significant refinement to dust modelling is necessary to ensure unbiased detection of CMB primordial B -modes at the precision required by future CMB experiments.

Acknowledgements. A.R. acknowledges financial support from the French space agency (Centre National d’Etudes Spatiales, CNES) and

the Italian Ministry of University and Research - Project Proposal CIR01_00010. F.B. acknowledges support from the Agence Nationale de la Recherche (project BxB: ANR-17-CE31-0022) and CNES. The authors would like to thank the anonymous referee for a thorough reading of the article and for all suggestions and comments that significantly improved the understanding of the text.

References

- Abazajian, K. N., Adshead, P., Ahmed, Z., et al., -S4 Science Book, First Edition. 2016, ArXiv e-prints, arXiv:1610.02743, [arXiv:1610.02743](#)
- Abitbol, M. H., Hill, J. C., & Johnson, B. R., Foreground-induced biases in CMB polarimeter self-calibration. 2016, MNRAS, 457, 1796
- Ade, P., Aguirre, J., Ahmed, Z., et al., The Simons Observatory: science goals and forecasts. 2019, J. Cosmology Astropart. Phys., 2019, 056
- Ade, P. A. R., Ahmed, Z., Amiri, M., et al., BICEP/Keck XV: The BICEP3 Cosmic Microwave Background Polarimeter and the First Three-year Data Set. 2022, ApJ, 927, 77
- Ashton, P. C., Ade, P. A. R., Angilè, F. E., et al., First Observation of the Submillimeter Polarization Spectrum in a Translucent Molecular Cloud. 2018, ApJ, 857, 10
- Azzoni, S., Abitbol, M. H., Alonso, D., et al., A minimal power-spectrum-based moment expansion for CMB B-mode searches. 2021, J. Cosmology Astropart. Phys., 2021, 047
- Benabed, K., Cardoso, J. F., Prunet, S., & Hivon, E., TEASING: a fast and accurate approximation for the low multipole likelihood of the cosmic microwave background temperature. 2009, MNRAS, 400, 219
- Bennett, C. L., Larson, D., Weiland, J. L., et al., Nine-year Wilkinson Microwave Anisotropy Probe (WMAP) Observations: Final Maps and Results. 2013, ApJS, 208, 20
- Chluba, J., Hill, J. C., & Abitbol, M. H., Rethinking CMB foregrounds: systematic extension of foreground parametrizations. 2017, Monthly Notices of the Royal Astronomical Society, 472, 1195
- Chon, G., Challinor, A., Prunet, S., Hivon, E., & Szapudi, I., Fast estimation of polarization power spectra using correlation functions. 2004, MNRAS, 350, 914
- de la Hoz, E., Diffuse polarized foregrounds from component separation with QUIJOTE-MFI. 2022, arXiv e-prints, [arXiv:2203.04861](#)
- Delouis, J. M., Pagano, L., Mottet, S., Puget, J. L., & Vibert, L., SRoll2: an improved mapmaking approach to reduce large-scale systematic effects in the Planck High Frequency Instrument legacy maps. 2019, A&A, 629, A38
- Désert, F.-X., The interstellar dust emission spectrum. Going beyond the single-temperature grey body. 2022, A&A, 659, A70
- Fixsen, D. J., Bennett, C. L., & Mather, J. C., COBE Far Infrared Absolute Spectrophotometer Observations of Galactic Lines. 1999, The Astrophysical Journal, 526, 207
- Górski, K. M., Hivon, E., Banday, A. J., et al., HEALPix: A Framework for High-Resolution Discretization and Fast Analysis of Data Distributed on the Sphere. 2005, ApJ, 622, 759

- Guillet, V., Fanciullo, L., Verstraete, L., et al., Dust models compatible with Planck intensity and polarization data in translucent lines of sight. 2018, A&A, 610, A16
- Guth, A. H., Inflationary universe: A possible solution to the horizon and flatness problems. 1981, Phys. Rev. D, 23, 347
- Haslam, C. G. T., Salter, C. J., Stoffel, H., & Wilson, W. E., A 408-MHz All-Sky Continuum Survey. II. The Atlas of Contour Maps. 1982, A&AS, 47, 1
- Hensley, B. S. & Bull, P., Mitigating Complex Dust Foregrounds in Future Cosmic Microwave Background Polarization Experiments. 2018, The Astrophysical Journal, 853, 127
- Hensley, B. S. & Draine, B. T., The AstroDust+PAH Model: A Unified Description of the Extinction, Emission, and Polarization from Dust in the Diffuse Interstellar Medium. 2022, arXiv e-prints, arXiv:2208.12365
- Ichiki, K., Kanai, H., Katayama, N., & Komatsu, E., Delta-map method of removing CMB foregrounds with spatially varying spectra. 2019, Progress of Theoretical and Experimental Physics, 2019, 033E01
- Kamionkowski, M. & Kovetz, E. D., The Quest for B Modes from Inflationary Gravitational Waves. 2016, ARA&A, 54, 227
- Krachmalnicoff, N., Carretti, E., Baccigalupi, C., et al., S-PASS view of polarized Galactic synchrotron at 2.3 GHz as a contaminant to CMB observations. 2018, A&A, 618, A166
- Linde, A., Scalar field fluctuations in the expanding universe and the new inflationary universe scenario. 1982, Physics Letters B, 116, 335
- LiteBIRD Collaboration, Allys, E., Arnold, K., et al., Probing Cosmic Inflation with the LiteBIRD Cosmic Microwave Background Polarization Survey. 2022, arXiv e-prints, arXiv:2202.02773, arXiv:2202.02773
- Mangilli, A., Aumont, J., Rotti, A., et al., Dust moments: towards a new modeling of the galactic dust emission for CMB B-modes analysis. 2021, A&A, 647, A52
- Martire, F. A., Barreiro, R. B., & Martínez-González, E., Characterization of the polarized synchrotron emission from Planck and WMAP data. 2022, J. Cosmology Astropart. Phys., 2022, 003
- Mennella, A., Bersanelli, M., Butler, R. C., et al., Planck early results. III. First assessment of the Low Frequency Instrument in-flight performance. 2011, A&A, 536, A3
- Osumi, K., Weiland, J. L., Addison, G. E., & Bennett, C. L., Limits on Polarized Dust Spectral Index Variations for CMB Foreground Analysis. 2021, ApJ, 921, 175
- Pelgrims, V., Clark, S. E., Hensley, B. S., et al., Evidence for line-of-sight frequency decorrelation of polarized dust emission in Planck data. 2021, A&A, 647, A16
- Planck Collaboration, Abergel, A., Ade, P. A. R., et al., Planck 2013 results. XI. All-sky model of thermal dust emission. 2014a, A&A, 571, A11
- Planck Collaboration, Abergel, A., Ade, P. A. R., et al., Planck intermediate results. XVII. Emission of dust in the diffuse interstellar medium from the far-infrared to microwave frequencies. 2014b, A&A, 566, A55
- Planck Collaboration, Adam, R., Ade, P. A. R., et al., Planck 2015 results. X. Diffuse component separation: Foreground maps. 2016a, A&A, 594, A10
- Planck Collaboration, Adam, R., Ade, P. A. R., et al., Planck intermediate results. XXX. The angular power spectrum of polarized dust emission at intermediate and high Galactic latitudes. 2016b, A&A, 586, A133
- Planck Collaboration, Adam, R., Ade, P. A. R., et al., Planck 2015 results - VIII. High Frequency Instrument data processing: Calibration and maps. 2016c, A&A, 594, A8
- Planck Collaboration, Ade, P. A. R., Alves, M. I. R., et al., Planck intermediate results. XXII. Frequency dependence of thermal emission from Galactic dust in intensity and polarization. 2015, A&A, 576, A107
- Planck Collaboration, Ade, P. A. R., Aghanim, N., et al., Planck 2013 results. IX. HFI spectral response. 2014c, A&A, 571, A9
- Planck Collaboration, Aghanim, N., Akrami, Y., et al., Planck 2018 results. V. CMB power spectra and likelihoods. 2020a, A&A, 641, A5
- Planck Collaboration, Aghanim, N., Ashdown, M., et al., Planck intermediate results. XLVI. Reduction of large-scale systematic effects in HFI polarization maps and estimation of the reionization optical depth. 2016d, A&A, 596, A107
- Planck Collaboration, Aghanim, N., Ashdown, M., et al., Planck intermediate results. L. Evidence of spatial variation of the polarized thermal dust spectral energy distribution and implications for CMB B-mode analysis. 2017, A&A, 599, A51
- Planck Collaboration, Aghanim, N., Ashdown, M., et al., Planck intermediate results. XLVIII. Disentangling Galactic dust emission and cosmic infrared background anisotropies. 2016e, A&A, 596, A109
- Planck Collaboration, Aghanim, N., Akrami, Y., et al., Planck 2018 results - VI. Cosmological parameters. 2020b, A&A, 641, A6
- Planck Collaboration, Aghanim, N., Akrami, Y., et al., Planck 2018 results - III. High Frequency Instrument data processing and frequency maps. 2020c, A&A, 641, A3
- Planck Collaboration, Aghanim, N., Ashdown, M., et al., Planck intermediate results - XLVIII. Disentangling Galactic dust emission and cosmic infrared background anisotropies. 2016f, A&A, 596, A109
- Planck Collaboration, Akrami, Y., Ashdown, M., et al., Planck 2018 results - XI. Polarized dust foregrounds. 2020d, A&A, 641, A11
- Planck Collaboration, Akrami, Y., Ashdown, M., et al., Planck 2018 results - IV. Diffuse component separation. 2020e, A&A, 641, A4
- Planck HFI Core Team, Ade, P. A. R., Aghanim, N., et al., Planck early results. IV. First assessment of the High Frequency Instrument in-flight performance. 2011, A&A, 536, A4
- Puglisi, G., Fabbian, G., & Baccigalupi, C., A 3D model for carbon monoxide molecular line emission as a potential cosmic microwave background polarization contaminant. 2017, MNRAS, 469, 2982
- Rosset, C., Tristram, M., Ponthieu, N., et al., *Planck* pre-launch status: High Frequency Instrument polarization calibration. 2010, A&A, 520, A13
- Svalheim, T. L., Andersen, K. J., Aurlen, R., et al., BeyondPlanck XV. Polarized foreground emission between 30 and 70 GHz. 2020, arXiv e-prints, arXiv:2011.08503, arXiv:2011.08503
- Tassis, K. & Pavlidou, V., Searching for inflationary B modes: can dust emission properties be extrapolated from 350 GHz to 150 GHz? 2015, MNRAS, 451, L90
- Thorne, B., Dunkley, J., Alonso, D., & Naess, S., The Python Sky Model: software for simulating the Galactic microwave sky. 2017, MNRAS, 469, 2821
- Vacher, L., Aumont, J., Montier, L., et al., Moment expansion of polarized dust SED: A new path towards capturing the CMB B-modes with LiteBIRD. 2022a, A&A, 660, A111
- Vacher, L., Chluba, J., Aumont, J., Rotti, A., & Montier, L., High precision modeling of polarized signals: moment expansion method generalized to spin-2 fields. 2022b, arXiv e-prints, arXiv:2205.01049
- Weiland, J. L., Addison, G. E., Bennett, C. L., Halpern, M., & Hinshaw, G., Polarized Synchrotron Foreground Assessment for CMB Experiments. 2022, The Astrophysical Journal, 936, 24
- Zonca, A., Thorne, B., Krachmalnicoff, N., & Borrill, J., The Python Sky Model 3 software. 2021, The Journal of Open Source Software, 6, 3783